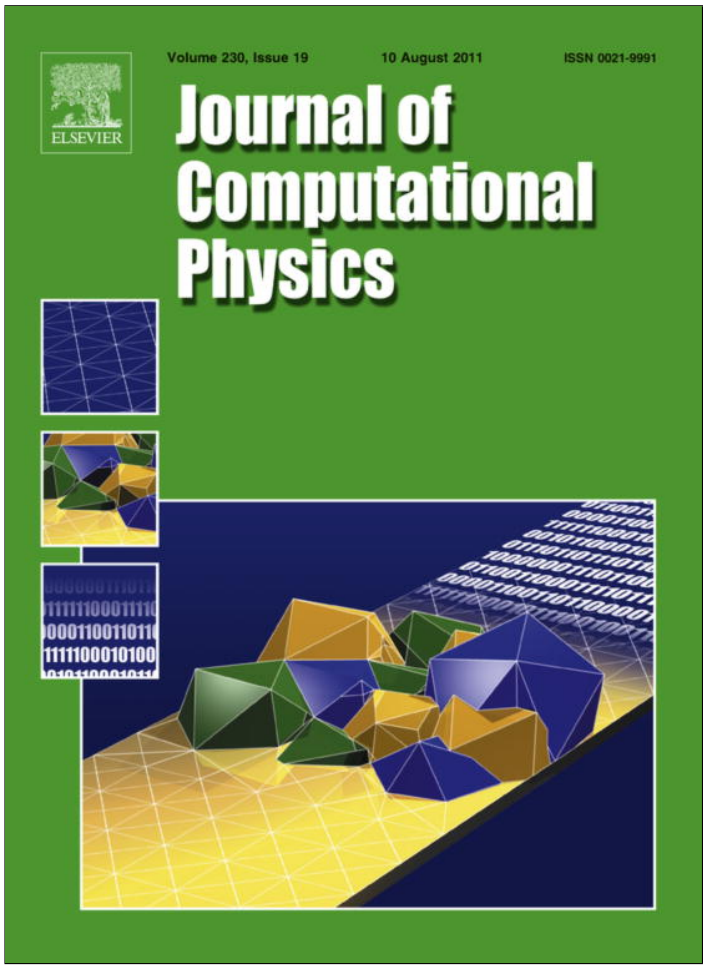

Journal of Computational Physics 230 (2011) 7266–7283

Contents lists available at ScienceDirect

Journal of Computational Physics

journal homepage: www.elsevier.com/locate/jcp

An efficient immersed boundary-lattice Boltzmann method for the hydrodynamic interaction of elastic filaments

Fang-Bao Tian [a,b,*], Haoxiang Luo [b], Luoding Zhu [c], James C. Liao [d], Xi-Yun Lu [a]

[a] Department of Modern Mechanics, University of Science and Technology of China, Hefei, Anhui 230026, China
[b] Department of Mechanical Engineering, Vanderbilt University, 2301 Vanderbilt Pl, Nashville, TN 37235-1592, USA
[c] Department of Mathematical Sciences, Indiana University-Purdue University Indianapolis, 402 North Blackford Street, Indianapolis, IN 46202, USA
[d] Whitney Laboratory for Marine Bioscience, Department of Biology, University of Florida, St. Augustine, FL 32080-8610, USA

ARTICLE INFO

Article history:
Received 7 July 2010
Received in revised form 24 March 2011
Accepted 24 May 2011
Available online 17 June 2011

Keywords:
Flow-structure interaction
Immersed boundary method
Lattice Boltzmann method
Fish swimming
Flapping flags

ABSTRACT

We have introduced a modified penalty approach into the flow-structure interaction solver that combines an immersed boundary method (IBM) and a multi-block lattice Boltzmann method (LBM) to model an incompressible flow and elastic boundaries with finite mass. The effect of the solid structure is handled by the IBM in which the stress exerted by the structure on the fluid is spread onto the collocated grid points near the boundary. The fluid motion is obtained by solving the discrete lattice Boltzmann equation. The inertial force of the thin solid structure is incorporated by connecting this structure through virtual springs to a ghost structure with the equivalent mass. This treatment ameliorates the numerical instability issue encountered in this type of problems. Thanks to the superior efficiency of the IBM and LBM, the overall method is extremely fast for a class of flow-structure interaction problems where details of flow patterns need to be resolved. Numerical examples, including those involving multiple solid bodies, are presented to verify the method and illustrate its efficiency. As an application of the present method, an elastic filament flapping in the Kármán gait and the entrainment regions near a cylinder is studied to model fish swimming in these regions. Significant drag reduction is found for the filament, and the result is consistent with the metabolic cost measured experimentally for the live fish.

1. Introduction

Flow-structure interaction (FSI) problems are ubiquitous in nature. Some examples include flapping flags, fish swimming, vocal fold vibration, and deformation of red blood cells. Addressing these problems typically requires coupling fluid dynamics and structural mechanics and solving the two components simultaneously. In addition, irregular geometries with large displacements are usually involved in these problems, making the mesh generation a challenging task. Therefore, capturing details of the FSI process through a numerical simulation is often computationally demanding.

A class of conventional numerical methods for the FSI is based on the body-fitted grid, and the moving grid is achieved through the arbitrary Lagrangian–Eulerian method [1]. In such methods, the grid may be distributed to provide adequate local resolution, but on the other hand, grid re-generation is usually needed every a few time steps to avoid severe mesh distortion. In contrast, the methods based on the non-body-conformal Cartesian grid such as the immersed boundary

* Corresponding author at: Department of Modern Mechanics, University of Science and Technology of China, Hefei, Anhui 230026, China.
E-mail address: tfbao@mail.ustc.edu.cn (F.-B. Tian).

0021-9991/$ - see front matter © 2011 Elsevier Inc. All rights reserved.
doi:10.1016/j.jcp.2011.05.028

method (IBM) and the lattice Boltzmann method (LBM) are much simpler in handling the complex and moving geometries and thus have received much attention in recent years.

The immersed boundary method developed first by Peskin [2] employs a boundary regularization approach. That is, the traction jump across a surface is distributed as a smooth body force onto the volumetric mesh in the vicinity of the surface, and the force is added in the Navier–Stokes equation to account for the effect of the surface. This method has been extended to model flow involving thin structures, bluff bodies, and fluid-fluid interfaces [3–5]. In addition to the diffuse-boundary approach, several other families of the IBM have been developed in which the sharp-interface representation of the solid surface is retained, e.g., the discrete-forcing approach adopting flow interpolation near the boundary [4] and the approach incorporating discontinuities in the solution across an immersed interface [6].

An alternative and robust method for fluid-flow simulations is the lattice Boltzmann method (LBM). Instead of discretizing the momentum equation, the LBM is an approach based on the particle kinetics. The method has achieved great success in the past decades and has proven to be an efficient solver for fluid flows. Readers are referred to the reviews by Chen and Doolen [7] and more recently by Aidun and Clausen [8] for the basic theory of this method. In the LBM, a popular scheme for FSI is based on the "bounce-back" rule to enforce the no-slip and no-penetration conditions at the solid surface. In the area of FSI, Ladd [9] first introduced bounce-back scheme to impose the fluid-structure coupling. Such a scheme is suitable for the rigid-body problems where the motion of the solid is determined only by the total force and torque exerting on the body [10,11]. However, when the boundary is flexible and the motion of the solid depends on the local hydrodynamic force, more effort is needed to inhibit the fluctuation of force acting on the structure [12,13].

To combine the advantage of the IBM for its simple boundary treatment and that of the LBM method for its fast flow simulation, hybrid methods coupling these two approaches have been developed recently. Among the various IBMs, Peskin's diffuse-boundary approach is particularly suitable for this combination, since in this approach all the grid points within the computational domain are treated with a unified equation. The standard LBM utilizing a uniform Cartesian mesh, was first combined with the IBM for handling the rigid moving particles by Feng and Michaelides [14,15]. After that, several versions of IB–LBM have been developed for the flow involving rigid bodies [16–18]. More recently, the IB–LBM has been extended to the simulation of elastic membranes [19,20] and plates [21,22], including both two and three dimensions.

As the standard LBM employs a uniform Cartesian mesh, the grid point distribution is thus not flexible, and the computational cost may become high when the Reynolds number is increased. To overcome this drawback, the multi-block LBM was developed [23,24], in which a fine-resolution Cartesian mesh overlaps with a background, coarse-resolution mesh to resolve the smaller spatial scales in the flow. Later, Sui et al. [25] combined the IBM with the multi-block LBM to model the interaction between an incompressible viscous fluid and elastic boundaries. To make efficient use of the grid points, an IB–LBM on the nonuniform Cartesian mesh was proposed by Wu and Shu [18] for simulating three-dimensional incompressible flows.

One particular issue of combining the IBM and LBM for simulations of FSI is to incorporate the inertia of the solid structure. Previous works [21,22,26] have not incorporated the mass effect of the structures. Explicitly including the inertial force in the IBM when calculating the hydrodynamic stress on the solid surface may easily destabilize the simulation. One way is to spread the mass of the solid into the bulk flow in the IBM method [3,27]. However, this approach does not work well with the LBM since the LBM assumes only a small variation of the fluid density when simulating incompressible flows. In the present work, we adopt the idea used in the penalty IBM proposed by Kim and Peskin [28], which is numerically robust while retaining the unified numerical description for the entire domain. The major contribution of the present work is to incorporate the penalty IBM into the multi-block IB–LBM for the FSI simulation of massive structures. The numerical approach is shown to be particularly efficient for solving the interaction of multiple thin-walled structures. Another contribution is that we have applied this approach to model the hydrodynamics of fish swimming in the vicinity of a bluff body and found a possible physical explanation for the observed fish behavior.

The organization of the paper is as follows. Section 2 briefly introduces the governing equations of the fluid and solid structures. The numerical approach is described in detail in Section 3. Section 4 presents several canonical examples to validate the accuracy of the present method. Demonstrations of the multi-filament simulation are given in Section 5. The study of a filament in the wake of a stationary cylinder is provided in Section 6. Final conclusions are given in Section 7.

2. Mathematical formulation

In the present LBM, the kinematics of the fluid is governed by the discrete lattice Boltzmann equation of a single relaxation time model [7,8,17,29],

$$g_i(\mathbf{x}+\mathbf{e}_i\Delta t, t+\Delta t) - g_i(\mathbf{x},t) = -\frac{1}{\tau}\left[g_i(\mathbf{x},\mathbf{t}) - g_i^{eq}(\mathbf{x},\mathbf{t})\right] + \Delta t G_i, \tag{1}$$

where $g_i(\mathbf{x},t)$ is the distribution function for particles with velocity $\mathbf{e}_i$ at position $\mathbf{x}$ and time t, Δt is the size of the time step, $g_i^{eq}(\mathbf{x},\mathbf{t})$ is the equilibrium distribution function, τ represents the nondimensional relaxation time, and G_i is the term representing the body force effect on the distribution function.

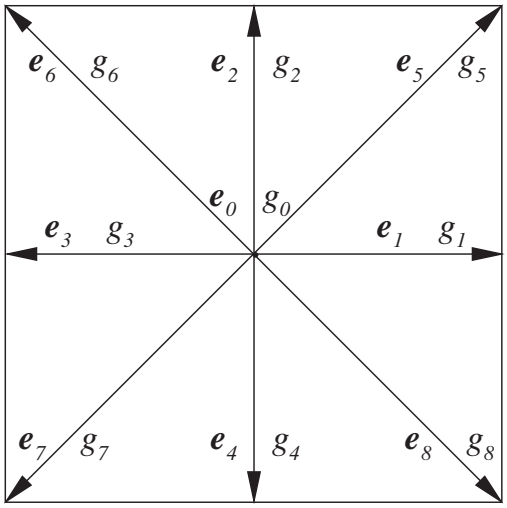

Fig. 1. Nine base vectors representing 9 possible velocity directions in the D2Q9 lattice model.

In the two-dimensional nine-speed (D2Q9) model, as shown in Fig. 1, the nine possible particle velocities are given by

$$\mathbf{e}_0 = (0,0),$$
$$\mathbf{e}_i = \left(\cos\frac{\pi(i-1)}{2}, \quad \sin\frac{\pi(i-1)}{2}\right)\frac{\Delta x}{\Delta t}, \quad \text{for } i = 1 \text{ to } 4,$$
$$\mathbf{e}_i = \left(\cos\frac{\pi(i-9/2)}{2}, \quad \sin\frac{\pi(i-9/2)}{2}\right)\frac{\sqrt{2}\Delta x}{\Delta t}, \quad \text{for } i = 5 \text{ to } 8,$$

where Δx is the lattice spacing. The values of $\mathbf{e}_i$ ensure that within one time step, a fluid particle moves to one of the eight neighboring nodes as shown in Fig. 1, or stays at its current location. In Eq. (1), g_i^{eq} and G_i are calculated according to [17,29]

$$g_i^{eq} = \omega_i \rho\left[1 + \frac{\mathbf{e}_i \cdot \mathbf{u}}{c_s^2} + \frac{\mathbf{uu} : (\mathbf{e}_i\mathbf{e}_i - c_s^2\mathbf{I})}{c_s^4}\right], \tag{2}$$

$$G_i = \left(1 - \frac{1}{2\tau}\right)\omega_i\left[\frac{\mathbf{e}_i - \mathbf{u}}{c_s^2} + \frac{\mathbf{e}_i \cdot \mathbf{u}}{c_s^4}\mathbf{e}_i\right] \cdot \mathbf{f}, \tag{3}$$

where ω_i are the weights given by $\omega_0 = 4/9$, $\omega_i = 1/9$ for $i = 1-4$ and $\omega_i = 1/36$ for $i = 5$–8, $\mathbf{u} = (u, v)$ is the velocity of the fluid, c_s is the speed of sound defined by $c_s = \Delta x/\sqrt{3}\Delta t$, and $\mathbf{f}$ is the body force acting on the fluid. The relaxation time is related to the kinematic viscosity in the Navier–Stokes equations in terms of

$$\nu = (\tau - 0.5)c_s^2\Delta t. \tag{4}$$

Once the particle density distribution is known, the fluid density, velocity and pressure are then computed from

$$\rho = \sum_i g_i, \tag{5}$$

$$\mathbf{u} = \frac{\sum_i \mathbf{e}_i g_i + \frac{1}{2}\mathbf{f}\Delta t}{\rho}, \tag{6}$$

$$p = \rho c_s^2. \tag{7}$$

The geometrically nonlinear motion for the filament is described as [30]

$$m_s\frac{\partial^2\mathbf{X}}{\partial t^2} - \frac{\partial}{\partial s}\left[T(s)\frac{\partial\mathbf{X}}{\partial s}\right] + K_b\frac{\partial^4\mathbf{X}}{\partial s^4} = \mathbf{F}_f, \tag{8}$$

where s is the Lagrangian coordinate along the length, $T(s) = K_s\left(\left|\frac{\partial\mathbf{x}}{\partial s}\right| - 1\right)$ is the tensile stress, K_s is the stretching coefficient, $\mathbf{X}$ is the position vector of a point on the filament, m_s is the linear density of the filament, K_b is the bending rigidity, and $\mathbf{F}_f$ is the hydrodynamic stress exerted by the fluid.

3. A modified penalty immersed boundary method

The immersed boundary method developed by Kim and Peskin [28] is extended here to handle the moving boundary. In this method, the boundary effect on the fluid is taken into account by spreading the surface force into the bulk fluid and treating it as a body force, which is done through the following expression,

$$\mathbf{f}(\mathbf{x},t) = \int \mathbf{F}(s,t)\delta_D(\mathbf{x}-\mathbf{X}(\mathbf{s},t))d\mathbf{s}, \tag{9}$$

where $\mathbf{F}(s,t)$ is the Lagrangian force density on the fluid by the elastic boundary, $\delta_D(\mathbf{x}-\mathbf{X}(\mathbf{s},t))$ is Dirac's delta function. The regularized body force is the same as $\mathbf{f}$ in Eq. (3), and it enters the kinetic equation of the fluid, Eq. (1), through G_i. Since $\mathbf{F}(s,t)$ is the reaction force of $\mathbf{F}_f$ in Eq. (8), it can be written as

$$\mathbf{F}(s,t) = -\mathbf{F}_d(s,t) + \mathbf{F}_e(s,t), \tag{10}$$

where $\mathbf{F}_d$ and $\mathbf{F}_e$ are the inertial force and elastic force, respectively, and are given by

$$\mathbf{F}_d(s,t) = m_s \frac{\partial \mathbf{U}(s,t)}{\partial t}, \tag{11}$$

$$\mathbf{F}_e(s,t) = \frac{\partial}{\partial s}\left[T(s)\frac{\partial \mathbf{X}}{\partial s}\right] - K_b\frac{\partial^4 \mathbf{X}}{\partial s^4}. \tag{12}$$

The velocity of a point on the filament is interpolated from the flow field, and the position of the filament is updated explicitly, i.e.,

$$\mathbf{U}(s,t) = \int \mathbf{u}(\mathbf{x},t)\delta_D(\mathbf{x}-\mathbf{X}(s,t))d\mathbf{x}, \tag{13}$$

$$\frac{\partial \mathbf{X}(s,t)}{\partial t} = \mathbf{U}(s,t), \tag{14}$$

where $\mathbf{U}(s,t)$ is the velocity of the filament. Note that Eqs. (10)–(14) are equivalent to those used by Zhu and Peskin [27].

The filament is discretized by N_f initially equally spaced nodal points, and the position of the mth node at time level n is denoted by $\mathbf{X}_m^n$. To compute the tensile force at mth node, a finite-difference scheme is used, i.e.,

$$\frac{\partial}{\partial s}\left[T(s)\frac{\partial \mathbf{X}}{\partial s}\right]_m = \frac{T_{m+\frac{1}{2}}\mathbf{t}_{m+\frac{1}{2}} - T_{m-\frac{1}{2}}\mathbf{t}_{m-\frac{1}{2}}}{\Delta s}, \tag{15}$$

where Δs is the grid spacing and the tension T and tangent vector, $\mathbf{t} = \partial\mathbf{X}/\partial s$, at the segment center, $m+\frac{1}{2}$, are both computed using a second-order central difference scheme. Note that Eq. (15) is nearly second-order accurate since the stretching ratio of the filament is low and the length difference between the consecutive segments is small. The bending force in Eq. (12) is also computed using a central difference scheme,

$$\frac{\partial^4 \mathbf{X}}{\partial s^4} = \frac{\mathbf{X}_{m+2} - 4\mathbf{X}_{m+1} + 6\mathbf{X}_m - 4\mathbf{X}_{m-1} + \mathbf{X}_{m-2}}{\Delta s^4}. \tag{16}$$

The discretizations of these elastic forces are the same as those in Zhu and Peskin [27].

The discretization of the inertial term, $\mathbf{F}_d(s,t)$, also known as the D'Alembert force, in Eq. (11) requires more care. One way to evaluate the temporal derivative in this equation is to apply an explicit finite difference scheme involving the current and previous time steps. However, it is known that such a scheme is numerically stable only for the extremely light filaments whose mass is lower than the critical value required for the flow-induced flapping [28]. Another approach is to estimate the temporal derivative of the velocity on the Cartesian mesh according to the momentum equation, and then interpolate the derivative onto the nodal points of the filament. However, our numerical results show that this approach also is effective only for the low-mass filaments.

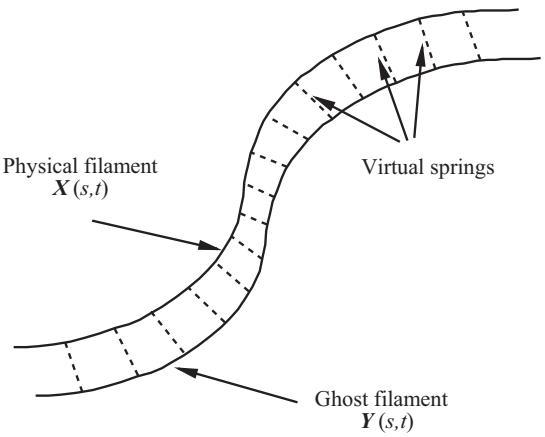

Fig. 2. The physical and ghost filaments are tethered together by virtual springs with a large stiffness K_t.

In the present simulations, the penalty immersed boundary method in [28] is adopted to calculate the inertial force and ensure the numerical stability. Specifically, the filament itself is assumed to be massless, but a second filament of linear density m_s is attached to the physical filament through virtual springs of stiffness K_v shown in Fig. 2. The second filament is termed "ghost filament" here, as it only affects the dynamics of the physical filament but is not seen by the flow solver directly. The FSI still takes place through the interface between the fluid and the physical filament. Eq. (10) is thus modified to incorporate the ghost filament,

$$\mathbf{F}(s,t) = \mathbf{F}_k(s,t) + \mathbf{F}_e(s,t), \tag{17}$$

$$\mathbf{F}_k(s,t) = K_v(\mathbf{Y}(s,t) - \mathbf{X}(s,t)), \tag{18}$$

$$m_s \frac{\partial^2 \mathbf{Y}}{\partial t^2} = -\mathbf{F}_k, \tag{19}$$

where $\mathbf{F}_k$ is the spring force, K_v is the stiffness of virtual springs, and $\mathbf{Y}(s,t)$ is the position vector of the point on the ghost filament connecting to point $\mathbf{X}(s,t)$ on the physical filament. Essentially, the effect of the inertia of the ghost filament is cushioned through the virtual springs. The second equation in Eq. (19) is discretized as

$$m_s \frac{\mathbf{Y}^{n+1} - 2\mathbf{Y}^n + \mathbf{Y}^{n-1}}{\Delta t^2} = -\mathbf{F}_k^n. \tag{20}$$

A three-step approach [31] is employed to treat Eqs. (13) and (14), which is described as

$$\mathbf{U}^* = \int \mathbf{u}^n(\mathbf{x})\delta_D(\mathbf{x} - \mathbf{X}^n)d\mathbf{x}, \quad \mathbf{X}^* = \mathbf{X}^n + \Delta t\mathbf{U}^*, \tag{21}$$

$$\mathbf{U}^{**} = \int \mathbf{u}^n(\mathbf{x})\delta_D(\mathbf{x} - \mathbf{X}^*)d\mathbf{x}, \quad \mathbf{X}^{**} = \frac{3}{4}\mathbf{X}^n + \frac{1}{4}\mathbf{X}^* + \frac{1}{4}\Delta t\mathbf{U}^{**}, \tag{22}$$

$$\mathbf{U}^n = \int \mathbf{u}^n(\mathbf{x})\delta_D(\mathbf{x} - \mathbf{X}^{**})d\mathbf{x}, \quad \mathbf{X}^{n+1} = \frac{1}{3}\mathbf{X}^n + \frac{2}{3}\mathbf{X}^{**} + \frac{2}{3}\Delta t\mathbf{U}^n. \tag{23}$$

The advantage of this approach is that the computation is more stable when the stretching coefficient K_s is high and the filament is nearly inextensible.

In the IBM, a smooth approximation [3] of Dirac's delta function, δ_h, is used,

$$\delta_h(\mathbf{x}) = \frac{1}{\Delta x \Delta y}\phi\left(\frac{x}{\Delta x}\right)\phi\left(\frac{y}{\Delta y}\right), \tag{24}$$

$$\phi(r) = \begin{cases} \left(3 - 2|r| + \sqrt{1 + 4|r| - 4r^2}\right)/8, & |r| < 1, \\ \left(5 - 2|r| - \sqrt{-7 + 12|r| - 4r^2}\right)/8, & 1 \leqslant |r| < 2, \\ 0, & |r| \geqslant 2. \end{cases} \tag{25}$$

For the lattice Boltzmann simulations, $\Delta x = \Delta y$ is used.

The stretching coefficient K_s is chosen to be large enough so that the stretching ratio of the structure is less than 5%. Such a ratio is allowed because an exceedingly large K_s could make the simulation unstable. In our simulations, we adopt $K_s/(\rho U^2 L) = O(10^2)$, where U is the characteristic velocity and L is the length of the unstretched filament. Similarly, K_v is chosen to ensure that the simulations are stable while the distance between the physical and ghost filaments does not vary significantly. Consider the spring–ghost filament a simple harmonic oscillator whose intrinsic frequency $\lambda = \sqrt{K_v/m_s}$ depends on the spring stiffness as well as the mass of the ghost filament. In our simulation, the dimensionless λ is chosen such as $(\lambda L/U)^2 = O(10^3)$.

In addition to elastic filaments, rigid bodies of finite thickness are also incorporated in the present method to study the interaction between the elastic and rigid bodies. To handle a rigid surface of general shape, we use the following method to calculate the boundary force on stationary surface [27],

$$\mathbf{F}(s,t) = -K_{st}(\mathbf{X}(s,t) - \mathbf{X}(s,0)), \tag{26}$$

where K_s is the artificial stiffness coefficient of the body.

The multi-block LBM proposed by Yu et al. [23] is employed in this study to simulate the flow. The computational domain is divided into several blocks which are connected through the interface between the blocks. The exchange of variables at the interface is done so that the mass and momentum are conserved and the stress is continuous across the interface. Suppose that a coarse lattice with spacing Δx_c overlaps with a fine lattice with spacing Δx_f. In order to keep a consistent viscosity in both blocks, the relation between the relaxation times, τ_c (on the coarse-mesh block) and τ_f (on the fine-mesh block), should be $\tau_f = 1/2 + m(\tau_c - 1/2)$, where $m = \Delta x_c/\Delta x_f$. Furthermore, to keep the variables and their derivatives continuous across the interface between the blocks, the density distribution functions for the coarse and fine blocks are described as

$$\tilde{g}_i^{(c)} = g_i^{(eq,f)} + m\frac{\tau_c - 1}{\tau_f - 1}\left[\tilde{g}_i^{(f)} - g_i^{(eq,f)}\right], \tag{27}$$

$$\tilde{g}_i^{(f)} = g_i^{(eq,c)} + \frac{\tau_f - 1}{m(\tau_c - 1)}\left[\tilde{g}_i^{(c)} - g_i^{(eq,c)}\right]. \tag{28}$$

In the present simulations, the immersed solid bodies are covered by the fine mesh only, and the solid surface does not cut through the mesh interface.

It is important to mention that the present method is limited to flows with low Reynolds numbers. Such low-*Re* limitation is generally shared by the immersed-boundary methods that regularize the boundary singularity by smearing the fluid–solid interface [4]. Finally, the current numerical method is presented for two-dimensional (2D) problems. However, the method can be easily extended to the three-dimensional (3D) problems involving elastic boundaries as previous IB–LB methods [22,32]. More specifically, the immersed boundary can be treated in the same way as in [21], the inertial force of the elastic structure can be calculated using the ghost element as described here, and the LBM simulation can be done in the same way as in [32].

4. Validation of the numerical method

Four problems with previously established results are used to validate the numerical algorithm described in Section 3: (1) laminar flow past a stationary cylinder, (2) vortex-induced vibration of a cylinder, (3) a single filament flapping in a uniform flow, and (4) interaction of two filaments placed side by side. These problems cover stationary and moving boundaries, as well as rigid and elastic bodies, so the successful validation will provide support for our later studies of the filament–filament and filament–rigid body interactions.

4.1. Laminar flow past a stationary cylinder

Viscous flow past a stationary cylinder is one of the canonical examples for testing accuracy of a numerical method. As shown in Fig. 3, this flow is solved here to assess the accuracy of the present modified penalty IB–LBM solver. Simulations are performed for Re = 20, 40, 60, 80, 100 and 200 on a $40d \times 20d$ domain, where Re is the Reynolds number based on the free-stream velocity, U, and the diameter of the cylinder, d. The computational domain is discretized by a two-block Cartesian mesh. One is a uniform grid around the cylinder with the block size of $25d \times 6d$ and the resolution $\Delta x = \Delta y = 0.02d$. The other is a uniform grid covering the outer region with a coarser resolution, $\Delta x = \Delta y = 0.04d$. Table 1 shows the average drag coefficient $C_D = F_D/(\frac{1}{2}\rho U^2 d)$ and the Strouhal number $St = fd/U$, where F_D is the mean drag force on the cylinder and f is the vortex shedding frequency. The results from several sources are listed in the table for comparison. It can be seen that our simulations are in good agreement with the other results.

To study the grid convergence of the present method, we perform a simulation test with the finest grid, $\Delta x = 0.01d$, and use the obtained result as the reference solution. Then we perform several cases with coarser resolutions and calculate the L_2 and L_∞ norms of the numerical error in the fluid velocity. In all cases, we set $\Delta s = 0.6\Delta x$, where Δs is the spacing of the marker points on the cylindrical surface. The convergence is shown in Fig. 4(a), where the error norms for both the u and v components in general exhibit a first-order accuracy. This convergence performance is consistent with the previous penalty IBM [28]. Therefore, combining the lattice Boltzmann simulation with the present boundary formulation has not compromised the numerical accuracy of the IBM. In some previous LBM studies using the implicit kernel, as in Ref. [17], nearly second-order accuracy was shown for flows in the absence of immersed bodies. In the present work, the accuracy is limited by the thin diffuse-boundary treatment, which is discussed in more detail by Refs. [28,36]. To demonstrate that the effect of the current boundary treatment, we calculate the error distribution of the u-velocity for the $\Delta x/d = 0.04$ mesh, and the result shows that the error concentrates around the surface of the cylinder (Fig. 4(b)).

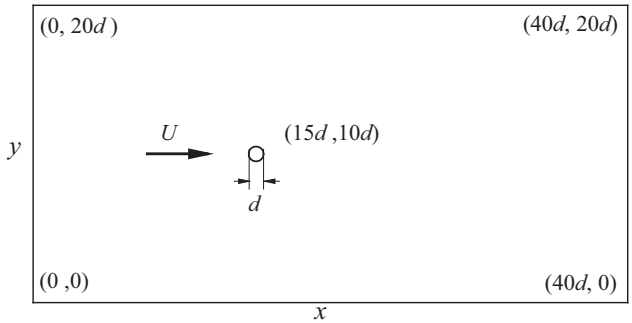

Fig. 3. Geometry for flow passing a stationary cylinder.

Table 1
Comparison of the mean drag coefficient, C_D, and Strouhal number, St, with previous data for the flow past a stationary cylinder.

Re	C_D/St (Present)	C_D/St [33]	C_D/St [34]	C_D/St [35]
20	2.16/–	2.09/–	2.04/–	2.23/–
40	1.62/–	1.58/–	1.54/–	1.66/–
60	1.49/0.138	1.44/0.143	–/–	–/–
80	1.44/0.155	1.40/0.158	1.40/0.150	–/–
100	1.43/0.166	1.39/0.169	1.39/0.160	1.42/0.171
200	1.44/0.198	1.39/0.204*	-/-	1.42/0.202

* The $Re = 200$ case in this column was simulated by using the same code from the authors of Ref. [33].

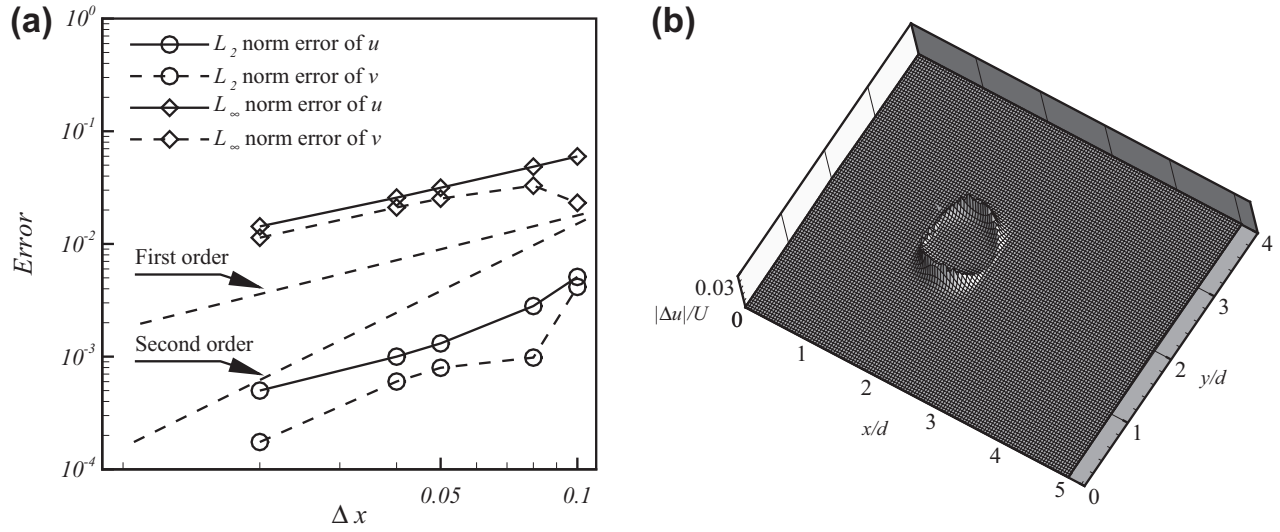

Fig. 4. (a) Convergence of the present numerical method. (b) Error distribution for the u-velocity.

4.2. Vortex-induced vibration of a cylinder

The vortex-induced vibration of a cylinder under subcritical Re is chosen to validate the present method for the flow–structure interaction problems involving rigid bodies. The cylinder immersed in a uniform freestream flow is mounted on two elastic supports and is free to vibrate in both the streamwise and transverse directions. The cylinder is subject to the hydrodynamic force and also the spring forces, and its dynamics is described as

$$m\frac{d^2\mathbf{X}_c(t)}{dt^2} + k\mathbf{X}_c(t) = \mathbf{F}_R, \tag{29}$$

where $\mathbf{X}_c$ denotes the displacement of the center of the cylinder, k is the stiffness of the supporting springs, m is the mass of the cylinder, and $\mathbf{F}_R$ is the resultant hydrodynamic force. The mesh in the simulation has a resolution of $\Delta x/d = \Delta y/d = 0.02$. The nondimensional mass and the reduced natural frequency of the spring–cylinder system are $M = 4m/(\pi\rho d^2) = 4.73$ and $F_n = \frac{d}{2\pi U}\sqrt{\frac{k}{m}} = 3.1875/Re$, respectively. Here the relationship between F_n and Re is imposed as done in Ref. [37].

The amplitude of the vibration in the transverse direction, Y_c/d, as a function of Re is shown in Fig. 5. The corresponding natural frequency, defined as $U^* = 1/F_n = Re/3.1875$, is also provided. The result from Mittal and Singh [37] is given for comparison. Although there is notable difference between the two results, the overall trends are consistent with each other. The lower critical Re predicted by the present method is between 19 and 20, and the upper critical Re is between 31 and 32. The critical Re in Mittal and Singh [37] is about 21.7 for the lower bound and 34 for the upper bound. In addition, the resonant vibration takes place at a slightly lower Re in our simulation, and the amplitude of the cylinder displacement is 8% higher than that in Mittal and Singh [37].

To make sure that the present result has converged, we performed two series of simulations, one with coarser resolution $\Delta x/d = \Delta y/d = 0.04$ and the other with finer resolution $\Delta x/d = \Delta y/d = 0.01$. In addition, a third series were done with a single-block mesh with $\Delta x/d = \Delta y/d = 0.02$ to make sure that the multi-block LBM is properly handled. These results are also shown in Fig. 5, from which it can be seen that grid-convergence has been reached and the single-block mesh gives a consistent result. To explain the difference by approximately 10% between our result and that of Mittal and Singh [37], we point out that the critical Reynolds number for a stationary cylinder varies between 45.4 and 50 and the critical Strouhal number varies between 0.12 and 0.14 depending on the specific numerical method used in the previous simulations [38,39]. In comparison, the current difference is comparable and is deemed acceptable.

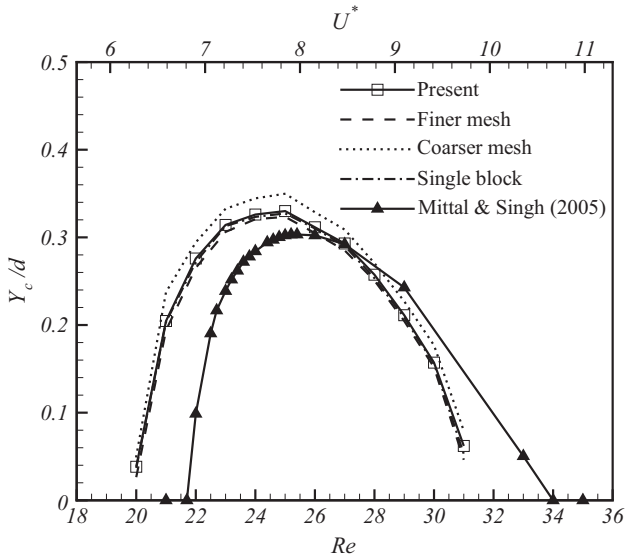

Fig. 5. The amplitude of the transverse oscillation in the vortex-induced cylinder vibration.

4.3. A single filament flapping in a uniform flow

We further consider a lone filament flapping in a uniform flow. The rigidity of the filament, E_b, defined by $K_b/(\rho U^2 L^3)$, is set to be on order of 10^{-4}. At this level, the filament vibration is no longer sensitive to E_b [30]. The mass ratio, defined by $S = m_s/\rho L$, where m_s is the linear density of the filament, ρ is the fluid density, and L is the length of the filament, is an important parameter in this problem. Both theoretical and numerical studies [27,40,30] have shown that a low-mass filament in the uniform flow tends to be more stable than a high-mass filament. In addition, a massless filament is always stable even in the presence of large perturbations [27]. In our simulation, we have obtained the similar conclusions. For a quantitative comparison, we have computed the critical mass ratio S_c, at which the filament exhibits a transition from a stable state to an unsteady flapping state at $Re = 90$ based on the filament length. In our simulations, S_c is determined between 0.22 and 0.28, which is in good agreement with the critical value $S_c = 0.26$ predicted by Connell and Yue [30]. The snapshots of the flow structures for $S = 0.22$ and $S = 0.28$ are shown in Fig. 6, and the flow patterns are consistent with those in Refs. [27,30].

4.4. Interaction between two flapping filaments

The interaction between two identical flapping filaments was studied experimentally [41,42], theoretically [42], and numerically [43,44]. In our simulation, the mass ratio and Reynolds number are chosen as $S = 0.3$ and $Re = 100$, respectively.

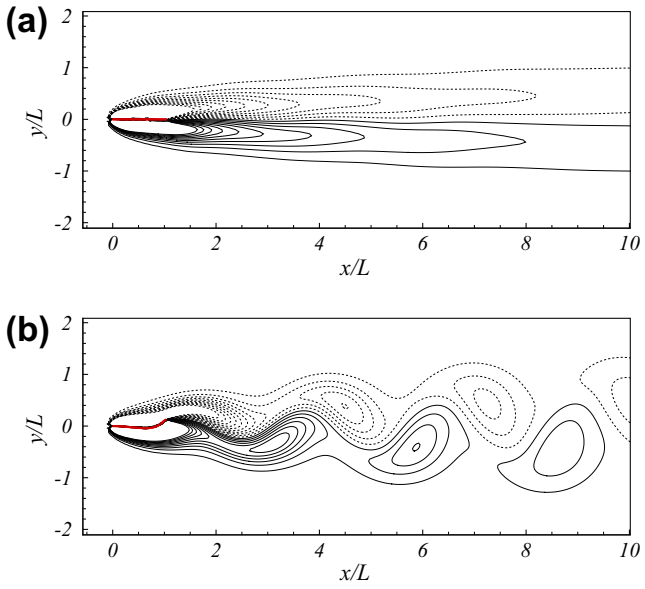

Fig. 6. Flow-induced flapping of a lone filament. The instantaneous vorticity field for (a) $S = 0.22$ and (b) $S = 0.28$ at $t\,U/L = 80$.

Simulations are performed for $D/L = 0.1$, 0.4 and 0.6, where L is the length of the filaments and D is the distance between them. The same mesh as in Section 4.1 is used here. The nondimensional bending rigidity, E_b, is the same as those in Section 4.3. A small-amplitude sinusoidal perturbation was introduced to the initial configuration of the filaments, where the amplitude increases from 0 at the leading edge to $0.1L$ at the trailing edge.

Fig. 7 shows the instantaneous vorticity field of the flow and also the deformation pattern of the filaments. For the small-gap case, $D/L = 0.1$, the two filaments settle down to an in-phase flapping state after several oscillations, and the flapping state is insensitive to the initial configuration of the two filaments. For example, even if the two filaments have initially anti-phase deformations, they will still approach the in-phase state after a few flapping cycles. The Strouhal number, defined by $St = fL/U$, is 0.29 in this case. When the filament separation distance becomes larger, $D/L = 0.4$, the filaments settle down to an anti-phase flapping state after a transient period. The Strouhal number is 0.38 during this state, which is approximately 28% higher than that of the in-phase case. The difference in the flapping frequencies of the two modes obtained here is consistent to the previous numerical and experimental studies [41,43]. In the experiment by Zhang et al. [41], where the Reynolds number is 20000, the difference between the two modes is 35%. In the numerical simulation at $Re = 200$ by Zhu and Peskin [43], where the flow is confined in a channel of width $2.4L$, this frequency increase is 41%. If the filament separation distance is further increased to $D/L = 0.6$, the phase between the filaments becomes irregular. The phenomenon is also observed in the previous work [41–43].

5. interaction of multiple filaments

Several explanations for the formation of fish schools have been proposed from different perspectives, including both the hydrodynamics-related ones, e.g., energy saving, and also others such as protection, socialization, genetics, and foraging [45,46]. Being able to model the interaction of multiple flexible bodies will allow us to investigate the schooling behavior of fish from a hydrodynamic point of view. Note that a filament passively flapping in flow can be very different from a swimming fish, which undulates its body by muscular activation. However, it was found that fish do make use of passive hydrodynamics in unsteady flow for energetic advantages [47]. Thus, the current filament model provides an extremely simplified yet illuminating representation of what could happen when the fish passively respond to the surrounding fluid.

In this section, we will study the characteristic dynamics of three filaments in a side-by-side arrangement and of ten filaments in a diamond arrangement. When a filament is located in the downstream wake of another filament, it may

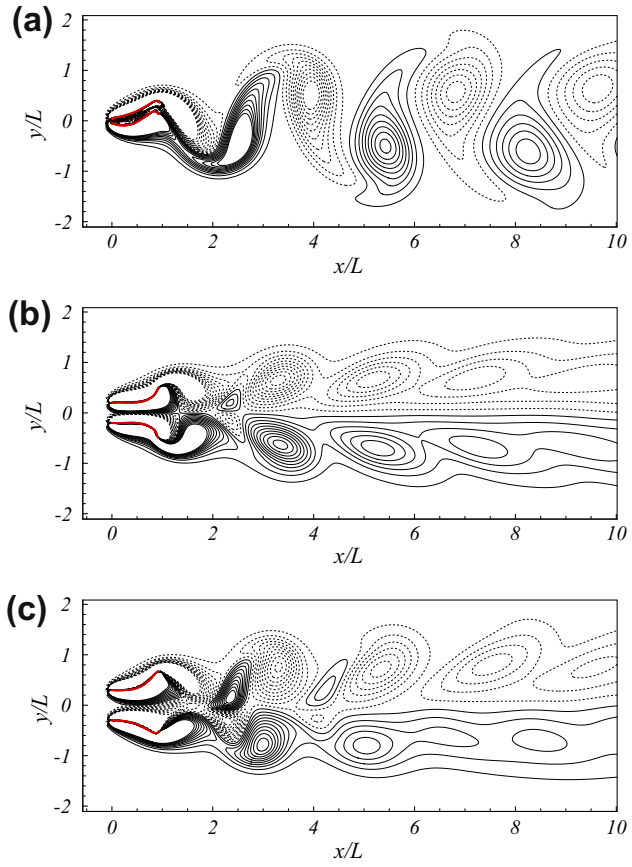

Fig. 7. Interaction between two identical flapping filaments in a side-by-side arrangement. The vorticity field for (a) $D/L = 0.1$, (b) $D/L = 0.4$, and (c) $D/L = 0.6$ at $tU/L = 160$.

experience exceedingly large deformations (e.g., a 180° bend). To avoid the situation, the bending rigidity of the filaments, $E_b = K_b/(\rho U^2 L^3)$, is set to be on order of 10^{-3}, i.e., one order of magnitude higher than that in the previous section. The Reynolds number and mass ratio in this section are $Re = 100$ and $S = 0.3$, respectively.

5.1. Three filaments in side-by-side arrangement

Interaction of the three filaments placed side by side as shown in Fig. 8 is significantly different from that of the two filaments due to the possibility for appearance of more coupling modes [48]. Previous linear stability analysis [48] and experimental study [49] showed that there exist at least three coupling modes when the filaments are separated within the range of hydrodynamic interaction. These modes are the in-phase mode, the symmetrical mode, and the out-of-phase mode.

Simulations were carried out to model the three filaments beyond the small-amplitude vibration. As shown in Fig. 8, three filaments of the same length L are placed side by side with spacing D. An initial sinusoidal displacement is set for the filaments with the amplitude growing from 0 at the leading edge to $0.1L$ at the trailing edge.

The simulated vibration mode and the vorticity field are shown in Fig. 9 for $Re = 100$ and four separation distances, $D/L = 0.1$, 0.2, 0.4, and 4.0. Note that in the present and also the earlier two-filaments configurations, it is physically possible for the filaments to collide with each other when the filaments are closely separated. Fortunately, the collision did not happen in the current simulations, which is likely due to the low Reynolds number considered and also due to the current diffuse-boundary treatment.

For the closest separation, $D/L = 0.1$, the filaments flap in phase in the same way as the two closely separated filaments described in Section 4.4, and the flapping pattern is independent of the phases of the initial displacements of the filaments (Fig. 9(a)). At this in-phase mode, the filaments are flapping like one single filament with the increased mass ratio. For a lone filament in an infinite flow, the flapping amplitude increases as the mass ratio S is raised. Therefore, the three filaments would have a higher deformation amplitude than the corresponding single filament. To make a quantitative assessment, we define the flapping amplitude as the root-mean-square value of the lateral displacement of the filament tail, $A = \sqrt{\frac{1}{T}\int_0^T (y - y_0)^2 \mathrm{d}t}$, where y_0 is the average y-position of the tail and T is the sampling duration. We use A_0 to denote the flapping amplitude of the corresponding single filament, which is $A_0/L = 0.13$ according to our simulation. Here the flapping amplitude of the filament 1, 2, and 3 is $A/A_0 = 1.98$, 2.05, and 1.92, respectively, where the inner filament has a slightly higher amplitude than the other two.

If the separation distance is increased to $D/L = 0.2$, the two outer filaments are in opposite phase, as shown in Fig. 9(b), and the amplitudes of the three filaments are, in their order, $A/A_0 = 0.77$, 0.43, and 0.76, which are significantly lower than 1. In particular, the vibration of the inner filament is reduced by more than 50% compared to the corresponding single filament. For $D/L = 0.4$, the two outer filaments are also in opposite phase, but filament 2 becomes virtually stationary, as shown in Fig. 9(c). At this distance, the three-filament system, as well as the flow field, exhibit a symmetrical pattern. The three flapping amplitudes are $A/A_0 = 0.87$, 0.02, and 0.86.

If the separation distance is further increased to $D/L = 4.0$, the inner filament starts to flap again, and its amplitude is almost the same as that of the other two filaments, as shown in Fig. 9(d). In addition, the inner filament is out of phase with the outer two filaments which, on the other hand, flap in phase with each other. The three flapping amplitudes are all at $A/A_0 = 1.0$. That is, the flapping amplitude is the same as that of the corresponding single filament. Note that the coupling modes shown in Fig. 9(a,c,d) are identified as the in-phase, symmetrical, and out-of-phase mode, respectively, and these coordinated patterns are consistent with those predicted by linear theory [48] and also those observed in the experiment [49]. Detailed quantitative comparison of the present result with the previous studies is not sought because the linear analysis [48] assumes a potential flow and the Reynolds number in the experiment [49] is $O(10^5)$ and is beyond the capability of the present code.

In addition to the same modes as reported previously, transient modes such as that shown in Fig. 9(b) for $D/L = 0.2$ and erratic flapping as reported in Alben [44] for two filaments are also observed in present simulations. These additional modes are currently under an in-depth investigation.

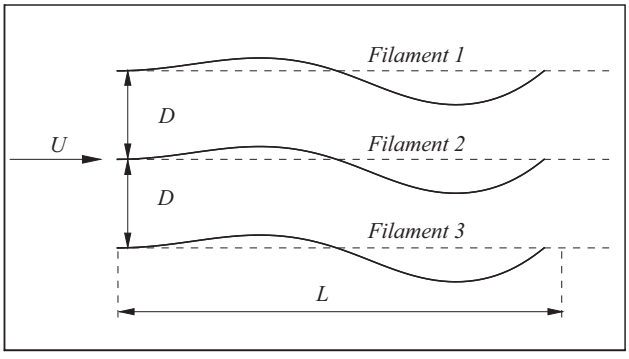

Fig. 8. Schematic of three filaments in a side-by-side arrangement.

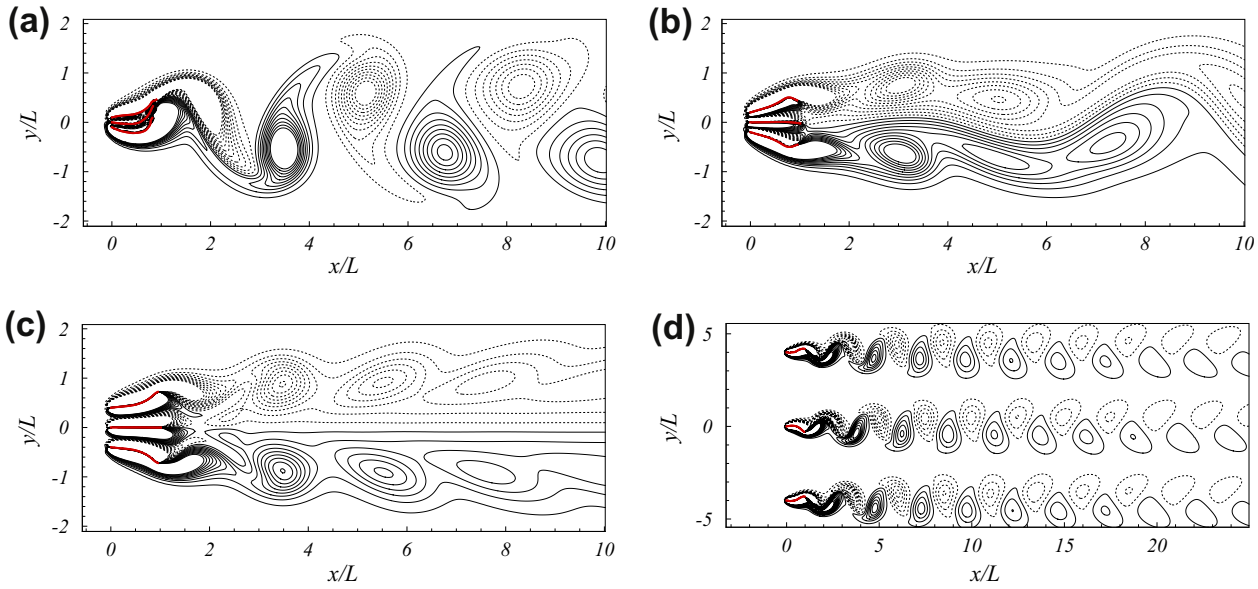

Fig. 9. Interaction between three identical filaments in side-by-side arrangement. The vorticity field for (a) $D/L = 0.1$, (b) $D/L = 0.2$, (c) $D/L = 0.4$, and (d) $D/L = 4.0$.

5.2. Ten filaments in diamond arrangement

To further show the capability of the present method, we consider an array of identical filaments organized in a staggered form shown in Fig. 10. A total number of ten filaments are arranged in the so-called "diamond" pattern, which has been observed in fish schools [50]. Previous studies of such a pattern focused on the prescribed fish motion and assumed that all the fishes undulate with the same amplitude, frequency, wave number, and phase [46]. The study of the completely passive undulation induced by the flow may provide insight into the question whether some fish in the school may take advantage of the passive flapping for energy saving. Ristroph and Zhang [51] performed an experimental study of six filaments in tandem arrangement. It was found that the six filaments flap with different amplitudes and the drag also differs for each filament.

In the present simulation, the filaments shown in Fig. 10 are placed such that $a/L = 4.0$ and $b/L = 2.0$. All the filaments have the same small-amplitude deformation pattern in the beginning of the simulation. The relative flapping amplitude of each filament is shown in Fig. 10. It can be seen that the downstream filaments have a significantly higher amplitude than the three leading filaments, whose amplitudes in turn are moderately higher compared to the isolated single filament. Substantial vortex–vortex and vortex–filament interactions can be observed via the flow visualization. An example of such interactions are shown by the instantaneous flow field in Fig. 11. The vortices shed from the upstream filaments merges into the vortices around the filaments that are located directly downstream, and the vortex merging changes the shedding behavior

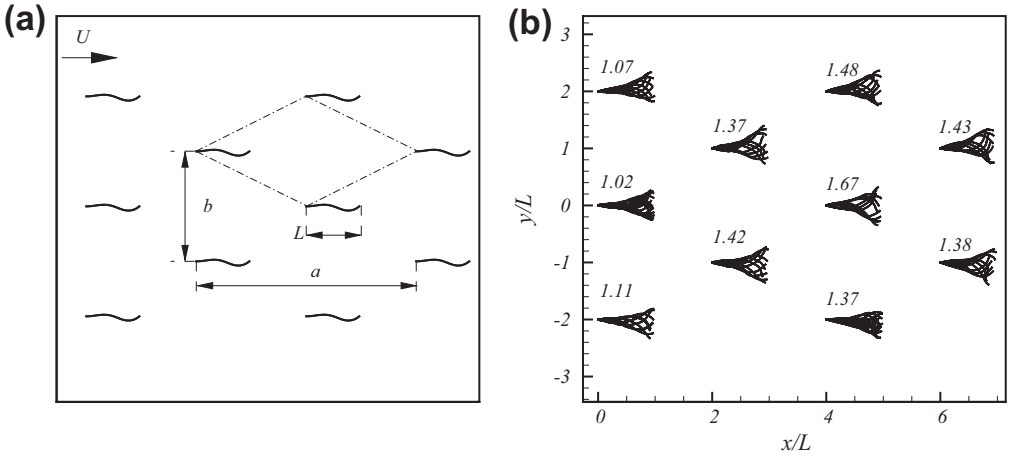

Fig. 10. (a) Schematic of ten filaments in the diamond arrangement. (b) Superimposed deformation patterns, where the numbers are the relative flapping amplitude, A/A_0, of the filaments.

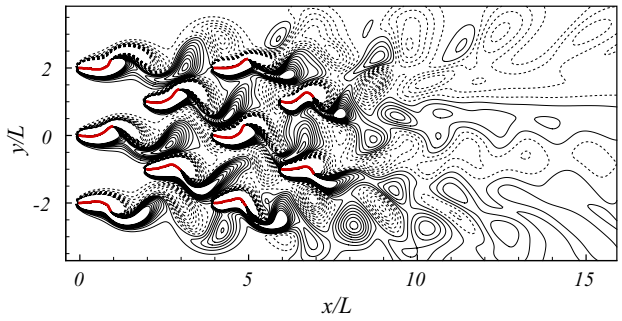

Fig. 11. The instantaneous vorticity field for the ten-filament arrangement.

of the downstream filament. In addition, the shed vortices also affect those filaments diagonally behind the upstream filaments by enhancing their vibration amplitude. Due to the vortex interaction, the wake behind the entire school exhibits an irregular form, and the flapping motion of the last filaments contains higher wavenumber deformations. The overall passive motions of the filaments appear to be well coordinated. That is, the dominant flapping frequency is the same for all the filaments, and the phase lags among the filaments, though not constants, vary slowly and in a generally consistent manner. Rich dynamics of the filaments can be observed. For example, some of the filaments may oscillate periodically with a large amplitude for a few cycles, then they appear to be suppressed for a short while, and then later they resume their large flapping magnitude.

Note that even though the present simulation is only two dimensional, it involves a highly irregular and moving geometry. Using the current IB–LBM method, the multi-filament simulation only takes about 60 hours for a time duration of $t = 2000L/U$, or around 500 flapping cycles, on a single Intel Xeon CPU E5520. Therefore, the efficient computation will allow us to extensively investigate the system behavior in the current problem.

6. A filament in the wake of a stationary cylinder

Fish swimming in the wake of a stationary bluff body may harness the kinetic energy from the vortices generated by the body [47,52]. Previously, the interaction between a flexible structure and a rigid cylinder has been employed to model the fish problem and understand the hydrodynamic benefit that the fish may enjoy [53–55]. In the present work, we consider an elastic filament placed either directly behind the cylinder, or in the shear layer on one side of the cylinder. These two regions are also referred to as the Kármán gait region and the entrainment region [56,57].

The problem configuration is shown by the schematic in Fig. 12. A filament of length L and linear density m_s is placed in the wake of a stationary cylinder of diameter d. The head of the filament is pinned while the tail is free. The streamwise distance between the fixed head and the center of the cylinder is G, and the distance between the fixed head and the centerline of the flow field is h. The computations are performed on the same domain and grid in Section 4.1. The Reynolds number based on the cylinder diameter is 100. The bending rigidity of the filaments, E_b, is again on order of 10^{-3} to prevent exceedingly large deformations.

In order to validate the present model, we conduct a laboratory experiment to measure the energetic cost of a live fish. A rainbow trout (*Oncorhynchus mykiss*) swims in a sealed, 175 liter flume respirometer (Loligo Systems Inc.) held at 15°C (Delta Chiller by Aqua Logic Inc., San Diego CA) with a working dimension of 25 cm × 25 cm × 87.5 cm. Two individuals are chosen

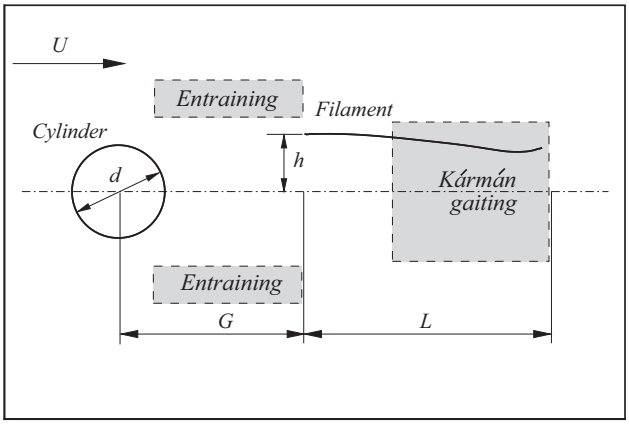

Fig. 12. Schematic of a filament in the wake of the cylinder.

to maximize the difference in the lateral dimension, L_w, defined as the average width in the dorsal view, while retaining similar dorso-ventral heights. Oxygen consumption is measured as an indication of the metabolic cost of swimming in the entrainment region and the free stream at a velocity of $3.5L\ s^{-1}$, where L is the total length of the fish. This value is referred to as the MO_2, which is normalized to the weight of the individual animal and has the units mg O_2/kg/hr. A 5 cm diameter cylinder is then placed in the sealed flume and fish are allowed to entrain volitionally. The position of the fish's head is recorded every minute in a six-hour experiment.

6.1. A filament in the Kármán gait region

First, we consider the filament placed directly behind the cylinder. In this region, rainbow trout adopt a distinctive swimming pattern called Kármán gait [57]. During this gait, the fish body amplitude and curvature are much larger than those of the fish swimming in the free stream, and the undulation frequency matches the vortex shedding frequency of the cylinder [57]. Previous studies using the model shown in Fig. 12 [58,25] have not incorporated the effect of the filament mass.

Simulations are performed for $G/d = 3$, $h/d = 0$. Several filament lengths and mass ratios are considered with $L/d = 1.0$, 2.5, 4.0, and $S = m_s/\rho d = 0.0$, 0.1 and 0.2. Note that the mass ratio has been re-defined using the diameter of the cylinder. The results show that for all the mass ratios, the filament is unstable, and a flapping motion is excited. This is in contrast with the a lone massless filament placed in uniform flow, where the filament would be stable [27,40]. The typical flapping motion of the filament is shown in Fig. 13(a). For the parameter regime considered here, the filament vibration is periodic.

Table 2 compares the averaged drag coefficient, C_D, the root-mean-square values of the lift coefficient of the cylinder, $C_{L,\mathrm{rms}}$, the drag ratio and amplitude of the filament, $C_{D,f}/C_{D,f0}$ and A/d, and the Strouhal number $St = f\,d/U$, where f is the flapping frequency of the filament. Here $C_{D,f}$ and $C_{D,f0}$ are, respectively, the drag coefficient of the filament and the drag coefficient of the corresponding single filament in the absence of the cylinder. Both coefficients are defined as the drag force normalized by $\frac{1}{2}\rho U^2 d$. In the present configurations, the filament flapping is induced by the vortices shed from the cylinder. Thus, the flapping frequency is identical to the frequency of the vortex shedding. Comparing the tabulated results for different mass ratios, we notice that for all three filament lengths, the mass ratio has little effect on the drag and lift of the cylinder, and the flapping frequency of the filament is not significantly affected either. However, the mass ratio has a significant effect on the flapping amplitude and drag of the filament. As S is raised from 0 to 0.2, A/d may increase up to 12% (e.g., for $L/d = 1.0$). Meanwhile, the drag ratio also becomes higher. Except for $L/d = 4.0$ and $S = 0.1$ and 0.2, the drag ratio is significantly below unity, indicating that the filament enjoys a drag reduction by staying behind the cylinder. For the two exceptional cases, we plot the flow field in Fig. 14. In these cases, the filament has a large bending deformation at its upstream portion, and its tail moves against the flow with a fast speed as the filament curls up. This inertial effect is more pronounced for $S = 0.2$, in which case, the drag on the filament is nearly 36% higher compared to the drag on the isolated filament.

Comparing the filaments with the same mass ratio but different lengths, we notice that filament length has only a slight effect on the forces of the cylinder, and the flapping frequency decreases within 8% as L/d increases from 1.0 to 2.5 and then to 4.0. On the other hand, the drag ratios and flapping amplitude are significantly higher for longer filaments. Therefore, we can conclude that within the parameter regime considered here, the flexible bodies with a lower mass ratio and a shorter length may benefit more from the interaction with the wake of the cylinder.

The effects of the mass ratio and length on the filament motion can also be seen from the trajectory of the free end of the filament (Fig. 13(b)). At $L/d = 1.0$, the filament flaps at a lower mode similar to that in Alben [59], where the tail end of filament follows an arc. At $L/d = 2.5$, the tail end traces out a "Fig. 8" path, a phenomenon also described in Shi and Phan-Thien [58], Sui et al. [25]. At $L/d = 4.0$, the trajectory combines the characteristics of those for $L/d = 1.0$ and $L/d = 2.5$, exhibiting an arched "Fig. 8".

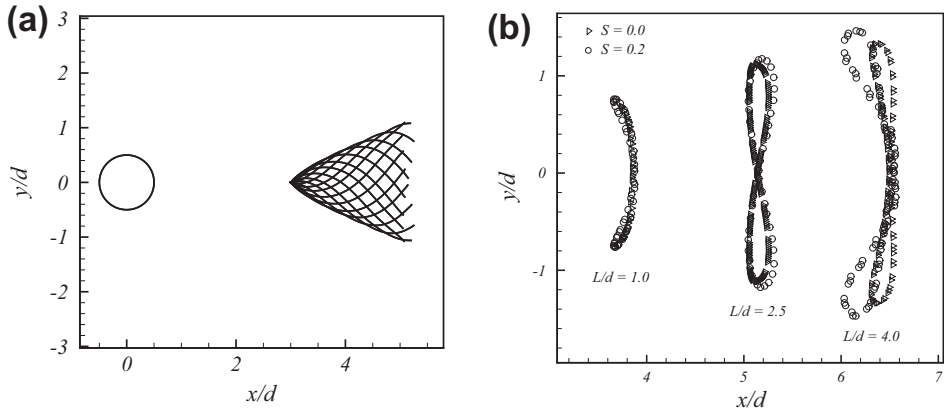

Fig. 13. (a) The profiles of a filament in the Kármán gait region. (b) Trajectory of the free end of the filament for $S = 0.0$ and 0.2 at $L/d = 1.0$, 2.5, and 4.0.

Table 2
Comparison of the flow characteristics for the filament in the Kármán gait region with $G/d = 3$.

A single cylinder	S	C_D	$C_{L,\mathrm{rms}}$	$C_{D,f}/C_{D,f_0}$	A/d	St
	–	1.44	0.25	–	–	0.166
L/d = 1.0	S = 0.0	1.43	0.27	0.38	0.69	0.161
	S = 0.1	1.42	0.26	0.47	0.73	0.161
	S = 0.2	1.42	0.26	0.58	0.77	0.153
L/d = 2.5	S = 0.0	1.40	0.28	0.60	1.11	0.156
	S = 0.1	1.40	0.27	0.73	1.14	0.155
	S = 0.2	1.39	0.26	0.87	1.18	0.153
L/d = 4.0	S = 0.0	1.39	0.29	0.79	1.34	0.153
	S = 0.1	1.39	0.30	1.02	1.42	0.153
	S = 0.2	1.39	0.31	1.36	1.46	0.152

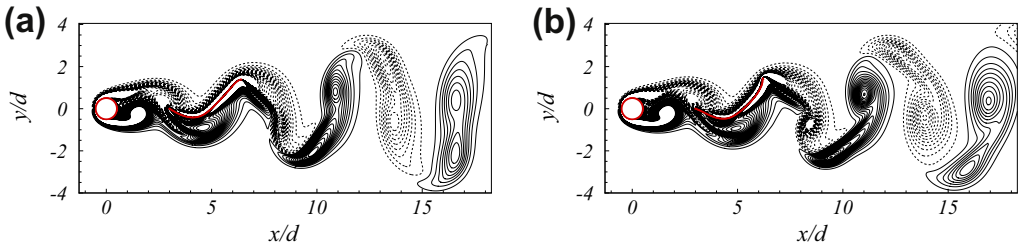

Fig. 14. The instantaneous vorticity field for the filament of in the Kármán gait region with $S = 0.1$ (a) and $S = 0.2$ (b).

6.2. A filament in the entrainment region

We now consider the situation where the filament is located in the entrainment region on either side of the cylinder. In this case, we set $G/d = 0.5$, and $h/d = 0.92$. Other parameters are the same as those in Section 6.1. The simulations are performed for $L/d = 2.5$ and $S = m_s/\rho d = 0.0$, 0.01, 0.1 and 0.2.

For the vanishing mass ratio, $S = 0.0$, the filament is nearly motionless. The vorticity contours of this case are shown in Fig. 15(a), where the vortex sheet on one side of the cylinder is clearly distorted due to presence of the filament. Note that the flow past a lone cylinder at this Reynolds number is not stable and vortex shedding would take place. The massless filament by itself is stable in an infinite flow. Thus, the filament in the present case apparently has stabilized the flow around the cylinder.

Due to the entrainment effect, the filament shape is slightly curved, and its tail bends into the wake of the cylinder, forming a small angle of attack. A similar phenomenon was observed in the real fish experiment by Liao [56], where the fish maintains its body and tail position but only moves pectoral fins for station keeping.

The temporal behavior of drag and lift coefficients for the cylinder with massless filament are presented in Fig. 15(b). Since the flow is not established in the beginning of the simulation and also there is an initial perturbation to the

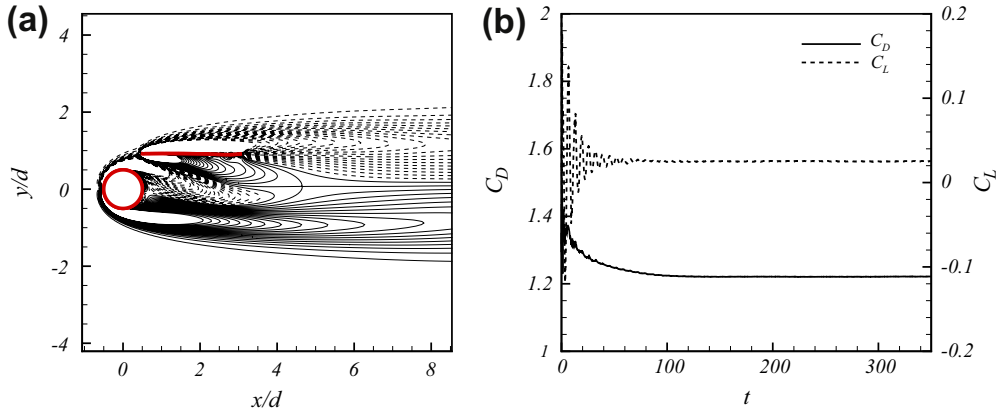

Fig. 15. The filament in the entrainment region. (a) The instantaneous vorticity field for $G/d = 0.5$, $h/d = 0.92$, $L/d = 2.5$, and $S = 0.0$. (b) Histories of the drag (C_D) and lift (C_L) coefficients of the cylinder.

configuration of the filament, the drag and lift oscillate during the transient stage. However, these forces quickly settle down to constant values. At the steady state, we obtained $C_D = 1.2$, which is smaller than the average drag of a single cylinder at $Re = 100$, $C_D = 1.4$. There is also a small lift force due to the flow asymmetry, pointing toward the filament side of the cylinder with $C_L = 0.03$.

To further investigate the stabilizing mechanism of the filament, we plot the profiles of the streamwise velocity, u, in the cylinder wake and compare them with the flow past a single cylinder. The results are shown in Fig. 16, where the profiles are shown at $x = 0.5d$ and $x = 3.0d$ from the cylinder center for the present case and also for a lone cylinder at $Re = 40$ and 100. It can be seen that the presence of the filament has changed the two shear layers around the cylinder and made the mean velocity profile in the shear layers closer to that for the lone cylinder case at $Re = 40$ than for the lone cylinder at $Re = 100$. This effect is true for both the near field ($x = 0.5d$) and the far field ($x = 3.0d$). Therefore, compared to the single cylinder, the effective Reynolds number of the shear layers is reduced and velocity profiles are more smeared when the filament is present. As a result, the flow around the cylinder is stabilized by the filament. To investigate the effect of h/d, we have performed a series of simulation with h/d varying from 0.8 to 1.5. The result shows that for h/d between 0.85 and 1.2, the massless filament suppresses the vortex shedding from the cylinder, and the filament itself is either stationary or has slight oscillations. Beyond this range, the filament is unable to stabilize the flow. Specifically, further reducing h/d would cause the filament to flap in the wake of the cylinder, and increasing h/d above 1.2 would lead to a weak interaction between the two objects.

When the mass ratio is increased, the flow becomes unsteady, and the filament starts to flap periodically. In addition, the flapping amplitude is higher for larger mass ratios. An instantaneous vorticity field for $S = 0.2$ is shown in Fig. 17(a). The vortices are shed alternately from the filament and from the other side of the cylinder. The negative vortex pinched off from the filament and the positive vortex from the cylinder form a sequence of vortex pairs in the wake. The flapping profiles of the filament are shown in Fig. 17(b). It can be seen that the filament of higher mass ratios in the entrainment region flaps asymmetrically. Note that at the current Reynolds number, all the corresponding single filaments, including $S = 0.2$, are stable in

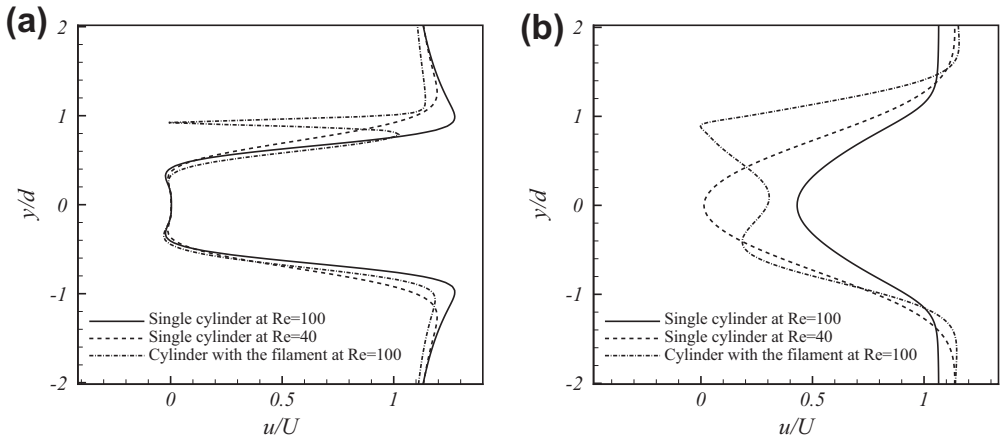

Fig. 16. Comparison of the mean streamwise velocity (u) profiles in the wake of the cylinder; (a) $x = 0.5d$ and (b) $x = 3.0d$ downstream from the cylinder center.

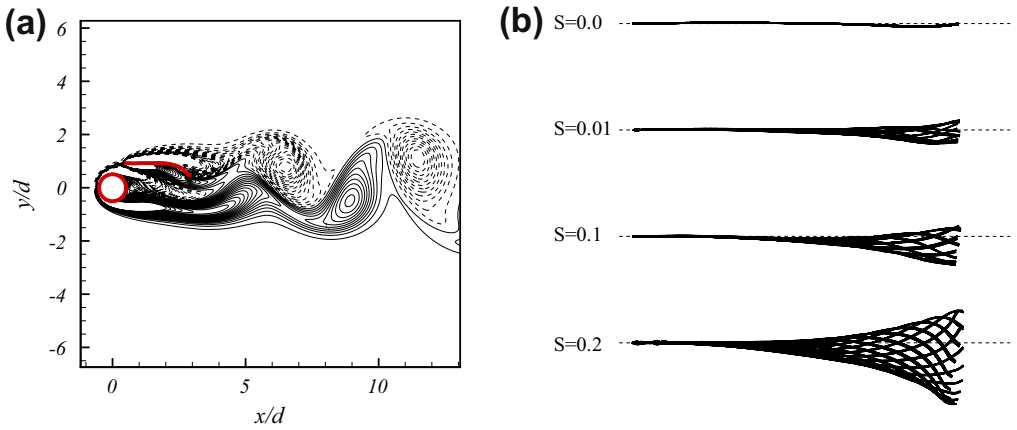

Fig. 17. The filament in the entrainment region. (a) The instantaneous vorticity field for $L/d = 2.5$, $G/d = 0.5$, $h/d = 0.92$ and $S = 0.2$. (b) The flapping pattern of the filament at different mass ratios.

Table 3
Comparison of flow characteristics for flow past a stationary cylinder with a filament in the entrainment region with $G/d = 0.5$ and $h/d = 0.92$. Here C_{D0} is the drag coefficient of the corresponding isolated cylinder.

L/d	S	C_D/C_{D0}	$C_{D,f}/C_{D,f0}$	A_m/d	St
1.5	0.0	0.86	0.91	0.00	–
	0.1	0.87	0.92	0.00	–
	0.2	0.87	0.94	0.16	0.145
2.5	0.0	0.85	0.81	0.00	-
	0.1	0.88	0.85	0.15	0.155
	0.2	0.89	0.93	0.36	0.157
4.0	0.0	0.86	0.76	0.16	0.128
	0.1	0.88	0.86	0.52	0.136
	0.2	0.89	0.96	0.70	0.131

the incident flow. One reason for the onset of such flapping motion is that the shear layer instability of the cylinder may overcome the stability effect of the filament. Another reason is that the filament in the shear layer of the cylinder is subject to a flow with higher velocity compared to the filament in an otherwise uniform flow and thus is more likely to become unstable.

The quantitative flow characteristics for different mass and length ratios are shown in Table 3. The drag coefficients of the cylinder and filament are both scaled by those of the isolated bodies. For the massless filament, the cylinder experiences a drag reduction of 15% compared to the lone cylinder, and the amount of reduction becomes slightly smaller when the mass ratio of the filament is higher. Increasing the filament length from $L/d = 1.5$ to $L/d = 4.0$ has little effect on the drag coefficient of the cylinder. In all the cases, the filament also enjoys a significant drag reduction compared to the corresponding isolated filament. For the massless filament, this reduction is 9% for $L/d = 1.5$ and increases to 24% for $L/d = 4.0$. At higher mass ratios, this drag benefit drops to less than 7% for all three filament lengths. The Strouhal number is not obviously affected by the mass ratio, but it varies by a small amount when the filament length is changed. Note that the Strouhal numbers shown here are close to those shown in Table 2, both are in turn close to the vortex shedding frequency of the corresponding isolated cylinder. Therefore, in both of the Kármán gait and entrainment regions, the flapping motion of the filament is dominated by the vortex shedding frequency of the cylinder.

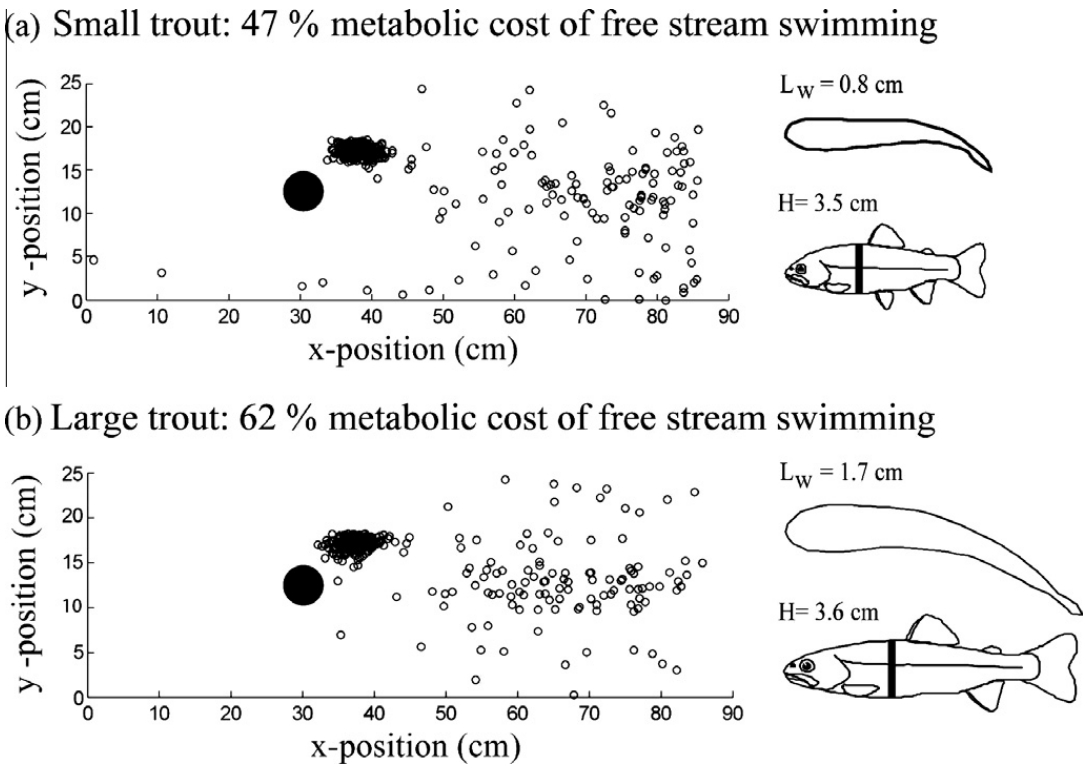

Fig. 18. (a) Plot of the head location for the small fish with $L_w = 0.8$ cm and $L = 17.7$ cm entraining behind a 5 cm diameter cylinder at $3.5L\ s^{-1}$ for every minute for 6 h. The fish entrains next to the cylinder for the majority of the experiment, occasionally exploring the Kármán vortex street and lateral sides of the flume downstream of the cylinder. The small fish uses 47% oxygen when entraining compared to swimming in the free stream. (b) The large fish ($L_w = 1.7$ cm and $L = 21.7$ cm) also entrains for the majority of the experiment, but compared to the small fish consumes a higher percentage of oxygen (62%) relative to the cost of the freestream swimming.

To summarize the numerical results of this section, we have found that the presence of the filament in the entrainment region tends to stabilize the flow around the cylinder, while on the other hand, the presence of the cylinder tends to destabilize the entraining filament. Furthermore, the entraining filaments with a lower mass ratio and a longer length would benefit more in drag reduction.

The complementary fish experiment is done as described in the beginning of this Section. Fig. 18 shows the head location of the fish collected for every minute for 6 h. It is immediately seen that the location markers are clustered in the entrainment region of the cylinder for fish of both sizes. We report the metabolic cost for entraining as a percentage of the metabolic cost for swimming in the free stream, normalized to the body mass. Remarkably, the small fish with $L_w = 0.8$ cm and $L/d = 3.5$ uses 47% oxygen when entraining compared to swimming in the free stream. The large fish $L_w = 1.7$ cm and $L/d = 4.3$ has less energy saving, but still uses up to 62% oxygen compared to the freestream swimming. Clearly, the fish benefits by spending time in the entrainment region. To draw a connection of the present numerical model with the hydrodynamics of real fish, we note that the density of the fish is close to that of water, and the mass ratio is approximately equal to the ratio between the average fish thickness and the length. Such a ratio is difficult to obtain accurately due to the three dimensionality and nonuniform distribution of the body mass. Since L_w is the average thickness of the body and is about 5% of the body length for the small fish and 8% for the large fish, we estimate that the mass ratios of both fish are within the range considered in the numerical model. Interestingly, the entraining fish does not undulate its body and maintains a steady position with its tail bent toward the wake of the cylinder, as reported in Liao [56], which is much like the massless filament presented here. The skewed body may act as a lift-producing foil to generate a lift force which prevents the fish from being drawn into suction region [56]. According to the numerical model, the entraining fish would experience a drag reduction compared to the freestream swimming. This prediction is consistent to the measurement of the fish energy consumption.

It should be pointed out the present filament model serves a crude representation of the fish hydrodynamics. There are several major differences between the model and the real fish swimming. For example, the body mass and material properties of fish are nonuniform, and the flow in nature is three dimensional. In addition, the Reynolds number in the experiment is on order of 10^4, which is much higher than that in the present simulation. Despite these important differences, the results presented here are consistent to the fish experiment and thus may serve as a physical explanation for the observed swimming behavior.

7. Conclusion

A numerical approach combining the immersed-boundary method and the multi-block lattice Boltzmann method is developed to simulate the interaction between multiple elastic structures and a viscous incompressible flow. More specifically, the surface force of the immersed bodies on the fluid is spread into the bulk region as a body force, and the fluid kinematics is simulated by solving the lattice Boltzmann equation. In addition, a penalty method is incorporated to handle the inertial force of the solid structures. Since grid regeneration is not required and directly solving the Navier–Stokes equation is avoided, the approach is extremely efficient for modeling the details of the coupled flow–structure interaction. Four benchmark computations are carried out to validate the present method: laminar flow past a stationary cylinder, vortex-induced vibration of a cylinder, a single filament flapping in a uniform flow, and interaction of two flapping filaments. The efficiency of the approach is demonstrated by simulations of multiple filaments passively flapping together in a uniform flow.

As an application, the filament in the wake of a cylinder is studied to model the Kármán gaiting and entraining behavior of fish near a bluff object. In the Kármán gait region directly behind the cylinder, the filaments with low mass ratios and short lengths enjoy more drag reduction compared to the filaments with high mass ratios and long lengths. In the entrainment region, i.e., the shear layer next to the cylinder, the filament may provide a stabilizing effect on the flow and maintain a steady position itself when the mass ratio is low. The entraining filaments also experience a significant drag reduction. However, unlike the Kármán gaiting filaments, the entraining filaments with a longer length receive more benefit. A complementary laboratory experiment is performed where the entraining behavior of the trout fish near a stationary cylinder is studied and the metabolic cost of the swimming is recorded. It is found that the fish benefit from entraining by significantly reducing oxygen consumption compared to the freesteam swimming. Furthermore, the fish tend to maintain a steady body position in the entrainment region. The numerical results are in general consistent with the experimental observation and may thus offer a physical insight to the biological behavior of the fish.

Acknowledgements

This work was supported by the National Science Foundation (No. CBET-0954381), the National Natural Science Foundation of China (No. 10832010), and the Innovation Project of the Chinese Academy of Sciences (No. KJCX2-YW-L05). Tian would like to acknowledge a fellowship support from the China Scholarship Council during his stay at Vanderbilt University.

References

[1] C.W. Hirt, A.A. Amsden, J.L. Cook, An arbitrary Lagrangian–Eulerian computing method for all flow speeds, J. Comput. Phys. 14 (1974) 227–253.
[2] C.S. Peskin, Flow patterns around heart valves: a digital computer method for solving the equations of motion, Ph.D. Thesis, Yeshiva University, 1972.
[3] C.S. Peskin, The immersed boundary method, Acta Numerica 11 (2002) 479–517.

[4] R. Mittal, G. Iaccarino, Immersed boundary method, Annu. Rev. Fluid Mech. 37 (2005) 239–261.
[5] S.O. Unverdi, G. Tryggvason, A front-tracking method for viscous, incompressible, multi-fluid flows, J. Comput. Phys. 100 (1992) 25–37.
[6] R.J. LeVeque, Z. Li, The immersed interface method for elliptic equations with discontinuous coefficients and singular sources, SIAM J. Numer. Anal. 31 (1994) 1019–1044.
[7] S. Chen, G.D. Doolen, Lattice Boltzmann method for fluid flows, Annu. Rev. Fluid Mech. 30 (1998) 329–364.
[8] C.K. Aidun, J.R. Clausen, Lattice-Boltzmann method for complex flows, Annu. Rev. Fluid Mech. 42 (2010) 439–472.
[9] A.J.C. Ladd, Numerical simulation of particulate suspensions via a discretized Boltzmann equation. Part 1: theoretical foundation, J. Fluid Mech. 271 (1994) 285–309.
[10] M. Krafczyk, J. Tölke, E. Rank, M. Schulz, Two-dimensional simulation of fluid-structure interaction using lattice-Boltzmann methods, Comput. Struct. 79 (2001) 2031–2037.
[11] P. Lallemand, L.S. Luo, Lattice Boltzmann method for moving boundaries, J. Comput. Phys. 184 (2003) 406–421.
[12] D. Qi, C.K. Aidun, A new method for analysis of the fluid interaction with a deformable membrane, J. Stat. Phys. 90 (1998) 145–158.
[13] A. Alexeev, R. Verberg, A.C. Balazs, Modeling the motion of microcapsules on compliant polymeric surfaces, Macromolecules 38 (2005) 10244–10260.
[14] Z.G. Feng, E.E. Michaelides, The immersed boundary-lattice Boltzmann method for solving fluid-particles interaction problems, J. Comput. Phys. 195 (2004) 602–628.
[15] Z.G. Feng, E.E. Michaelides, Proteus: a direct forcing method in the simulations of particulate flows, J. Comput. Phys. 202 (2005) 20–51.
[16] C. Shu, N. Liu, Y.T. Chew, A novel immersed boundary velocity correction-lattice Boltzmann method and its application to simulate flow past a circular cylinder, J. Comput. Phys. 226 (2007) 1607–1622.
[17] J. Wu, C. Shu, Implicit velocity correction-based immersed boundary-lattice Boltzmann method and its applications, J. Comput. Phys. 228 (2009) 1963–1979.
[18] J. Wu, C. Shu, An improved immersed boundary–lattice Boltzmann method for simulating three-dimensional incompressible flows, J. Comput. Phys. 229 (2010) 5022–5042.
[19] D.V. Le, J. White, J. Peraire, K.M. Lim, B.C. Khoo, An implicit immersed boundary method for three-dimensional fluid-membrane interactions, J. Comput. Phys. 228 (2009) 8427–8445.
[20] T. Krüger, F. Varnik, D. Raabe, Efficient and accurate simulations of deformable particles immersed in a fluid using a combined immersed boundary lattice Boltzmann finite element method, Comput. Math. Appl. 61 (2011) 3485–3505.
[21] J. Hao, L. Zhu, A lattice Boltzmann based implicit immersed boundary method for fluid-structure interaction, Comput. Math. Appl. 59 (2010) 185–193.
[22] L. Zhu, G. He, S. Wang, L. Miller, X. Zhang, Q. You, S. Fang, An immersed boundary method by the lattice Boltzmann approach in three dimensions with application, Comput. Math. Appl. 61 (2011) 3506–3518.
[23] D. Yu, R. Mei, W. Shyy, A multi-block lattice Boltzmann method for viscous fluid flows, Int. J. Numer. Meth. Fluids 39 (2002) 99–120.
[24] Y. Peng, C. Shu, Y.T. Chew, X.D. Niu, X.Y. Lu, Application of multi-block approach in the immersed boundary-lattice Boltzmann method for viscous fluid flows, J. Comput. Phys. 218 (2006) 460–478.
[25] Y. Sui, Y.T. Chew, P. Roy, H.T. Low, A hybrid immersed-boundary and multi-block lattice Boltzmann method for simulating fluid and moving-boundaries interactions, Int. J. Numer. Meth. Fluids 53 (2007) 1727–1754.
[26] J. Zhang, P.C. Johnson, A.S. Popel, An immersed boundary lattice Boltzmann approach to simulate deformable liquid capsules and its application to microscopic blood flows, Phys. Biol. 4 (2007) 285–295.
[27] L. Zhu, C.S. Peskin, Simulation of a flapping flexible filament in a flowing soap film by the immersed boundary method, J. Comput. Phys. 179 (2002) 452–468.
[28] Y. Kim, C.S. Peskin, Penalty immersed boundary method for an elastic boundary with mass, Phys. Fluids 19 (2007) 053103.
[29] Z.L. Guo, C.G. Zheng, B.C. Shi, Discrete lattice effects on the forcing term in the lattice Boltzmann method, Phys. Rev. E 65 (2002) 046308.
[30] B.S.H. Connell, D.K.P. Yue, Flapping dynamics of a flag in a uniform stream, J. Fluid Mech. 581 (2007) 33–67.
[31] Q.W. Shu, Essentially non-oscillatory and weighted essentially non-oscillatory schemes for hyperbolic conservation laws, ICASE Report No.97-65, 1997, pp. 325–432.
[32] Y. Sui, Y.T. Chew, P. Roy, H. Low, A hybrid method to study flow-induced deformation of three-dimensional capsules, J. Comput. Phys. 227 (2008) 6351–6371.
[33] T. Gao, Y.H. Tseng, X.Y. Lu, An improved hybrid cartesian/immersed boundary method for fluid-solid flows, Int. J. Numer. Meth. Fluids 55 (2007) 1189–1211.
[34] A.L.F. Lima E Silva, A. Silveira-Neto, J.J.R. Damasceno, Numerical simulation of two-dimensional flows over a circular cylinder using the immersed boundary method, J. Comput. Phys. 189 (2003) 351–370.
[35] S. Xu, Z.J. Wang, An immersed interface method for simulating the interaction of a fluid with moving boundaries, J. Comput. Phys. 216 (2006) 454–493.
[36] B.E. Griffith, C.S. Peskin, On the order of accuracy of the immersed boundary method: Higher order convergence rates for sufficiently smooth problems, J. Comput. Phys. 208 (2005) 75–105.
[37] S. Mittal, S. Singh, Vortex-induced vibrations at subcritical *Re*, J. Fluid Mech. 534 (2005) 185–194.
[38] M. Morzynski, F. Thiele, Numerical stability analysis of a flow about a cylinder, Z. Angew. Math. Mech. 71 (1991) T424–T428.
[39] B. Kumar, S. Mittal, Prediction of the critical Reynolds number for flow past a circular cylinder, Comput. Meth. Appl. Mech. Eng. 195 (2006) 6046–6058.
[40] M. Shelley, N. Vandenberghe, J. Zhang, Heavy flags undergo spontaneous oscillations in flowing water, Phys. Rev. Lett. 94 (2005) 094302.
[41] J. Zhang, S. Childress, A. Libchaber, M. Shelley, Flexible filaments in a flowing soap film as a model for one-dimensional flags in a two-dimensional wind, Nature 408 (2000) 835–839.
[42] L.B. Jia, F. Li, X.Z. Yin, X.Y. Yin, Coupling modes between two flapping filaments, J. Fluid Mech. 581 (2007) 199–220.
[43] L. Zhu, C.S. Peskin, Interaction of two flapping filaments in a flowing soap film, Phys. Fluids 15 (2003) 1954–1960.
[44] S. Alben, Wake-mediated synchronization and drafting in coupled flags, J. Fluid Mech. 641 (2009) 489–496.
[45] C.M. Breder, On the survival value of fish schools, Zoologica 52 (1967) 25–40.
[46] D. Weihs, Hydromechanics of fish schooling, Nature 241 (1973) 290–291.
[47] J.C. Liao, D.N. Beal, G.V. Lauder, M.S. Triantafyllou, Fish exploiting vortices decrease muscle activity, Science 302 (2003) 1566–1569.
[48] S. Michelin, S.G. Llewellyn Smith, Linear stability analysis of coupled parallel flexible plates in an axial flow, J. Fluids Struct. 25 (2009) 1136–1157.
[49] L. Schouveiler, C. Eloy, Coupled flutter of parallel plates, Phys. Fluids 21 (2009) 081703.
[50] M.H.S. Keenleyside, Some aspects in the schooling behavior in fish, Behaviours 8 (1955) 183–248.
[51] L. Ristroph, J. Zhang, Anomalous hydrodynamic drafting of interacting flapping flags, Phys. Rev. Lett. 101 (2008) 194502.
[52] J.C. Liao, A review of fish swimming mechanics and behaviour in altered flows, Phil. Trans. R. Soc. B 362 (2007) 1973–1993.
[53] D.N. Beal, F.S. Hover, M.S. Triantafyllou, J.C. Liao, G.V. Lauder, Passive propulsion in vortex wakes, J. Fluid Mech. 549 (2006) 385–402.
[54] J.D. Eldredge, D. Pisani, Passive locomotion of a simple articulated fish-like system in the wake of an obstacle, J. Fluid Mech. 607 (2008) 279–288.
[55] L.B. Jia, X.Z. Yin, Response modes of a flexible filament in the wake of a cylinder in a flowing soap film, Phys. Fluids 21 (2009) 101704.
[56] J.C. Liao, The role of the lateral line and vision on body kinematics and hydrodynamic preference of rainbow trout in turbulent flow, J. Exp. Biol. 209 (2006) 4077–4090.
[57] J.C. Liao, D.N. Beal, G.V. Lauder, M.S. Triantafyllou, The kármán gait: novel body kinematics of rainbow trout swimming in a vortex street, J. Exp. Biol. 206 (2003) 1059–1073.
[58] X. Shi, N. Phan-Thien, Distributed lagrange multiplier/fictitious domain method in the framework of lattice Boltzmann method for fluid-structure interactions, J. Comput. Phys. 206 (2005) 81–94.
[59] S. Alben, Simulating the dynamics of flexible bodies and vortex sheets, J. Comput. Phys. 228 (2009) 2587–2603.